

Incorporation of TiO₂ into the PtPd/C Catalyst Layer for Improvement ORR Activity and Water Management

Nutthaphak Kitiphapiboon¹, Mali Hunsom^{1,2,*}

¹ Fuels Research Center, Department of Chemical Technology, Faculty of Science, Chulalongkorn University, 254 Phayathai Road, Bangkok 10330, Thailand.

² Center of Excellence on Petrochemical and Materials Technology (PETRO-MAT), Chulalongkorn University, 254 Phayathai Road, Bangkok 10330, Thailand

*E-mail: mali.h@chula.ac.th

Received: 4 January 2016 / Accepted: 29 January 2016 / Published: 1 March 2016

Titanium dioxide (TiO₂) samples prepared by different thermal treatments were incorporated in the cathode catalyst layer of a polymer electrolyte membrane or proton exchange membrane (PEM) fuel cell. Increasing the TiO₂ treatment temperature (500–800 °C for 3 h) resulted in an increased rutile phase content and crystal size, but decreased textural properties of the obtained TiO₂. Incorporation of TiO₂ prepared at the appropriate temperature in the carbon-supported PtPd catalyst (PtPd/C) layer positively affected the catalyst dispersion, electrochemical surface area and electrical conductivity of catalyst layer, but did not affect the electron pathway of the oxygen reduction reaction (ORR) of PtPd/C catalysts. Overall, the PtPd/C catalyst with TiO₂ calcined at 800 °C (T₈₀₀-PtPd/C) exhibited the highest ORR activity (~486 mA/cm² at 0.6 V) both in an acid solution and in a PEM fuel cell under a H₂/O₂ environment at atmospheric pressure compared to those for the Pt/C, PtPd/C and the other TiO₂-PtPd/C catalysts.

Keywords: TiO₂, PtPd/C catalyst; ORR activity; PEM fuel cell

1. INTRODUCTION

Fuel cells are currently the most promising candidates to replace existing heat engines (i.e., internal combustion engines, steam turbines and gas turbines) for converting the energy contained in chemical feed stocks to electricity for energy utilizing plants and/or devices, from power plants to cars and homes [1]. Currently, research is being conducted into several types of fuel cells, such as alkaline, phosphoric acid, solid oxide, molten carbonate and polymer electrolyte membrane or proton exchange membrane (PEM) fuel cells. Some of them are already commercialized, while others are close to

commercialization. Among them, the PEM fuel cell demonstrates several desirable properties, including a low operation temperature requirement that makes them able to contain and reduce the thermal loss, their small size and light weight that makes them perfect for automotive and portable applications [1,2] and their relatively simple design and high conversion efficiency [3].

Although the low temperature operation can reduce the thermal loss and promote a quick start-up of PEM fuel cells, it reduces the rate of the electrochemical reaction, measured in terms of the exchange current density particular at the cathode side, and also reduces the mass transport properties of reactants and products in actual applications. To address the former problem, a high exchange current density catalyst, such as platinum (Pt) and its bimetallic alloy with another metal (Pt-M, where M = Pd, Cr, Co, Ni, Cu, Zr, Fe or Au) have been used [4–9]. Although some contradictory results for the ORR activity of bimetallic Pt alloys have been observed, most Pt-M catalysts were found to exhibit a superior electrocatalytic activity compared to a Pt catalyst [5], which was due to the geometric (bond distance) and electronic (*d*-band vacancy) effects resulting from the alloy formation [10]. The latter problems can be addressed by various approaches, such as using a high ionic conductive membrane to facilitate a fast proton transfer across the membrane electrolyte [11–14] or using high electronic conductive fuel cell components [15].

Another effective approach is the use of a dual- or multi-layer structured gas diffusion layer (GDL) in order to reduce the contact resistance between the catalyst layer and the macroporous carbon substrate by forming a flat and uniform layer, as well as improving the water management ability [16]. The incorporation of a microporous layer (MPL) in the GDL can reduce the liquid water saturation at the MPL/macroporous carbon substrate interface and also at the catalyst layer/MPL interface, and so reduces the severe water flooding [17], due to its higher hydrophobicity and lower porosity [18]. Increasing the polytetrafluoroethylene (PTFE), the hydrophobic agent, content in MPL on the carbon-fiber substrates resulted in an increased water flow resistance through the GDL due to the decreased MPL porosity and an increased volume fraction of hydrophobic pores [16]. An optimized PTFE content helped to reduce the oxygen transport limitation in the catalyst layer and GDL by controlling the liquid water saturation in the membrane electrode assemble (MEA). Using a more hydrophobic flow channel than the GDL induced more water accumulation on the GDL, which then dramatically affected the voltage from the PEM fuel cell [19]. Excess water in mini-flow channels, generated from the collision and coalescence of droplets, can directly form slugs in the PEM fuel cells, which can be alleviated by increasing the gas flow rate [20]. Incorporation of a suitable amount of Nafion[®] in the catalyst layer increased the three-phase boundary and electrochemical reaction sites [21], while sub-optimal Nafion[®] quantities led to a poor connection of the catalyst particles to the electrolyte and so a poor existence of three-phase boundary [22] as well as low conductivity [23]. However, super-optimal Nafion[®] levels prevented the flow of electrons dissociated at the catalyst to the GDL [22] and prevented efficient gas accessibility to the active sites to proceed the electrochemical reaction and promoted the electrode flooding [23].

In the present work, titanium dioxide (TiO₂) was selected due to its specific hydrophilic/hydrophobic properties [24,25] as well as having a large surface area and the presence of surface hydroxyl groups [26,27]. The TiO₂ was incorporated into the PtPd/C catalyst layer to form the

TiO₂-PtPd/C composite catalysts in order to potentially improve the ORR activity as well as the water management in PEM fuel cell.

2. EXPERIMENTAL

2.1. Preparation of TiO₂ in different phases

A series of TiO₂ samples were prepared by the thermal treatment of commercial TiO₂ (Degussa), a mixture of both anatase and rutile phases (T_{AR}), in air at different temperatures (500–800 °C) for 3 h. The obtained TiO₂ particles were ground and sieved to a size of smaller than 250 μm, and are herein designated as T_x, where x is the treatment temperature in °C. In addition, a commercial rutile phase TiO₂ (Aldrich) designed as T_R was included as a reference of the rutile phase.

2.2. Preparation of the PtPd/C electrocatalyst powder

The PtPd/C catalyst was prepared by the seeding and impregnation method according to the procedure described elsewhere [28]. At first, 4.4 mL of 20 g/L H₂PtCl₆ (Fluka) was mixed thoroughly with 2.78 mL of 20 g/L PdCl₂ (98%, Fluka). The pH of precursor solution was adjusted to 2 using 6 M HCl (Fluka). Approximately 10% (v/v) of this precursor solution was mixed with commercial carbon black (Vulcan XC-72), that had already been acid treated as previously reported [29], and then sonicated at 70 °C for 30 min. This was then slowly added by 20 mL of 1 M NaBH₄ (Alcan) and sonicated for 30 min at the same temperature to reduce the metal ions in solution. The obtained seeding powder was harvested by filtration and rinsed several times with hot de-ionized water (~70 °C) to eliminate the excess reducing agent. Afterwards, the seeding powder was dispersed in 10 mL de-ionized water and sonicated at 70 °C for 30 min before being mixed with the remaining PtPd solution at 90% (v/v) and continuously sonicated for 30 min. Approximately 20 mL of 1 M NaBH₄ was added slowly to reduce the Pt⁴⁺ and Pd²⁺ ions to their respective metals on the carbon support under sonication at 70 °C. The sonication was extended for 60 min to ensure the complete reduction of the metal ions. The formed PtPd/C catalysts were then separated from the solution by filtration, washed thoroughly with hot de-ionized water and then dried for 2 h at 100 °C. According to this procedure, the catalyst loading on the carbon support (PtPd/C) was around 40% (w/w).

2.3. Preparation of the catalyst ink and specimen for activity tests

The catalyst ink was prepared by dispersing 12.5 mg of the PtPd/C catalyst powder and 0.3 g of the respective TiO₂ in 0.5 mL isopropanol (98%, Fisher) into 0.22 mL of deionized water. The obtained slurry was sonicated at 100 °C for 2 h and then 100 mg of Nafion[®] 117 solution (5wt.%, Fluka) was added and sonicated at 4 °C for 5 min. To evaluate the respective catalyst activity test in an acid solution, the ink of TiO₂-PtPd/C catalyst was coated onto a 1-cm diameter circular carbon cloth (ETEK) using a spray gun (HKX-HB-3G) at identical loading of 0.15 mg/cm². The catalyst-coated

carbon cloth was then dried at 80 °C for 5 min to eliminate the solvent. To evaluate the respective catalyst activity in a single PEM fuel cell, the catalyst ink was coated onto the membrane in the same manner and loading (0.15 mg/cm²). The TiO₂-PtPd/C catalyst was loaded on the cathode and the commercial Pt/C (20 wt.%, ETEK) was loaded on the anode. The obtained catalyst-coated membrane was then assembled between two sheets of the carbon ink-coated GDL [9] and pressed together by a compression mold (LP20, Labtech) under 65 kg/cm² for 2.5 min at 137 °C to form the MEA.

2.4. ORR activity tests

The ORR activity of all the prepared catalysts was first tested in the acid solution. The catalyst-coated carbon cloth was mounted on the rotating disk electrode (RDE) and used as the working electrode. A Pt rod and Ag/AgCl electrode were used as the counter and reference electrodes, respectively. All electrodes were immersed in oxygen-saturated 0.5 M H₂SO₄ and connected with a Potentiostat/Galvanostat (AUTOLAB, PG STATO 30) via the linear sweep voltammetry (LSV). The potential of the system was varied from 0.25 to 0.80 V at constant scan rate of 10 mV/s and different rotation rates (range 500–2,000 rpm).

For the ORR activity test in a single PEM fuel cell, the MEA obtained from section 2.3 was mounted on commercial single-cell hardware (Electrochem, Inc.) and tested in a single cell test station [30]. The catalyst layer of the respective TiO₂-PdPt/C catalyst and the commercial Pt/C catalyst were used as the cathode and anode catalysts, respectively. Prior to testing the cell performance, the run-in stage was carried under an atmospheric pressure (1.0 psia) with a cell temperature of around 60 °C by feeding H₂ and O₂ at 100 sccm and the current was drawn at constant potential of 0.2 V for 12 h. Consequently, the performance of the single cell was monitored in the form of current density-potential curves (polarization curves), detected by a Potentiostat/Galvanostat at 60 °C and ambient pressure.

2.5. Characterization

The textural properties of each TiO₂ powder and respective TiO₂-PtPd/C catalysts were analyzed by a surface area analyzer (Quantachrome, Autosorb-1) according to the Brunauer-Emmett-Teller (BET) method. The qualitative surface functional group of TiO₂ was measured by Fourier Transform Infrared spectroscopy (FT-IR, PerkinElmer USA) using the potassium bromide (KBr) pellet method. The level of oxygen-containing surface functional groups on the TiO₂ was determined by Boehm's method [31,32]. The contact angle of TiO₂-PtPd/C catalysts was measured by Standard Contact Angle Goniometer (Rame'hart, 200-U1). The conductivity of each different TiO₂-PtPd/C catalysts was measured as an in-plane structure using a four point probe instrument (Jandel, RM3-AR) at 25 °C. The morphology of each electrocatalyst type was characterized by X-ray diffraction (XRD) analysis on a Bruker D8-Discover machine and by scanning electron microscopy (SEM) with energy dispersive X-ray analysis (SEM-EDX) on a JEOL JEM 6610LV. In addition, the electrochemical surface area (ECSA) of the catalyst layer was measured using the H₂ stripping method.

3. RESULTS AND DISCUSSION

3.1. Morphology of the TiO_2 and TiO_2 -PtPd/C catalysts

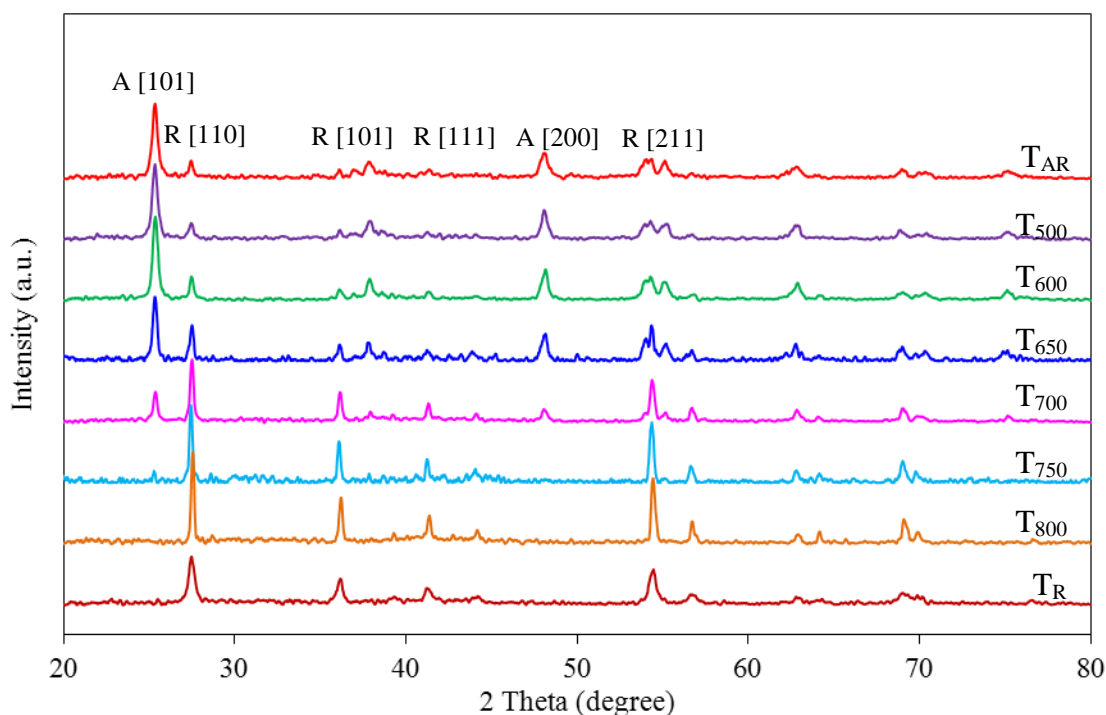


Figure 1. Representative XRD patterns of the commercial TiO_2 samples (T_{AR} and T_R) and the TiO_2 after treatment at different temperatures ($T_{500-800}$).

Fig. 1 exhibits representative XRD patterns of the untreated commercial mixed phase TiO_2 (T_{AR}) and after thermal treatment at different temperatures over the range of 500–800 °C (T_{500} to T_{800}). The XRD peaks of T_{AR} demonstrated the main characteristic peaks of the anatase phase at a 2θ of 25.32° and 47.76° and also the rutile phase at a 2θ of 27.42°, 36.02° and 53.56°, corresponding to the A[101], A[200], R[110], R[101] and R[211] planes, respectively. This confirms that the T_{AR} sample was a mixture of anatase and rutile phases. When the T_{AR} was subjected to treat at between 500-600 °C, almost the same XRD peaks were observed compared with the untreated sample, with anatase still the dominate phase. Increasing the treatment temperature above 600 °C resulted in a decreased intensity of the A[101] and A[200] peaks and an increased intensity of the R[110], R[101] and R[211] peaks, demonstrating the transformation of the anatase to rutile phase. Further raising the treatment temperature up to 800 °C resulted in the disappearance of all anatase peaks, indicating an almost complete transformation of anatase to rutile phase. Interestingly, at treatment temperature of 800 °C, these TiO_2 (T_{800}) samples demonstrated sharper characteristic peaks of the rutile phase than those of T_R , suggesting that T_{80} had a higher level of crystallinity than the commercial T_R .

The ratio of the peak intensity between the rutile and anatase phases obtained from the XRD analysis was used to compute the rutile content at each treatment temperature according to Eq. (1) [33];

$$R(T) = 0.679 \frac{I_R}{I_R + I_A} + 0.312 \left(\frac{I_R}{I_R + I_A} \right)^2 \quad (1)$$

where $R(T)$ is the content (%) of the rutile phase in TiO_2 , I_A is the peak intensity of the main [101] anatase peak and I_R is the peak intensity of the main [110] rutile peak.

From this analysis, the original commercial T_{AR} was found to be comprised of 13% rutile phase and this increased with increasing treatment temperatures, especially above 650 °C (Table 1). A marked transformation of the anatase to rutile phase was observed following treatment temperature at 600–800 °C, where the rutile phase content increased from 17 to greater than 99%.

Table 1. Properties of the commercial mixed phase TiO_2 before (T_{AR}) and after treatment at different temperatures ($T_{500-800}$), and that of the rutile phase TiO_2 (T_R).

Source	Treatment temperature (°C)	Symbol	Rutile content (%)	Particle size (nm)	BET surface area (m ² /g)	Micropore vol. (cm ³ /g)	Mesopore vol. (cm ³ /g)	Hydroxyl group (mEq/g)
TiO_2 (Degussa)	--	T_{AR}	14	23.0	62.9	0.0629	0.2112	3.565
	500	T_{500}	13	22.7	97.2	0.0745	0.2669	1.337
	600	T_{600}	17	24.7	54.7	0.0621	0.2201	1.285
	650	T_{650}	28	28.0	48.1	0.0483	0.1962	1.243
	700	T_{700}	60	33.4	39.1	0.0366	0.1146	0.514
	750	T_{750}	83	35.8	19.6	0.0214	0.0622	0.118
	800	T_{800}	99	39.0	17.2	0.0296	0.0883	0.030
TiO_2 (Aldrich)	--	T_R	99	20.0	37.0	0.0412	0.1661	1.444

The crystal size of all TiO_2 samples, as estimated by the Debye-Scherrer equation, also increased as the treatment temperature increased (Table 1). According to the textural properties of the TiO_2 samples, the T_{AR} had a BET surface area and micro- and meso-pore volumes of 62.9 m²/g, 0.0629 cm³/g and 0.2112 cm³/g, respectively. When subjected to the treatment temperature of 500 °C, these textural properties were all markedly increased, but increasing the treatment temperature above 500 °C resulted in a temperature-dependent decrease in all the textural properties (Table 1). This is probably due to the widening of existing pores or the combining of some neighboring pores as well as to the collapse of the existing pores at a high treatment temperature, and so causing a sharp decrease in the BET surface area.

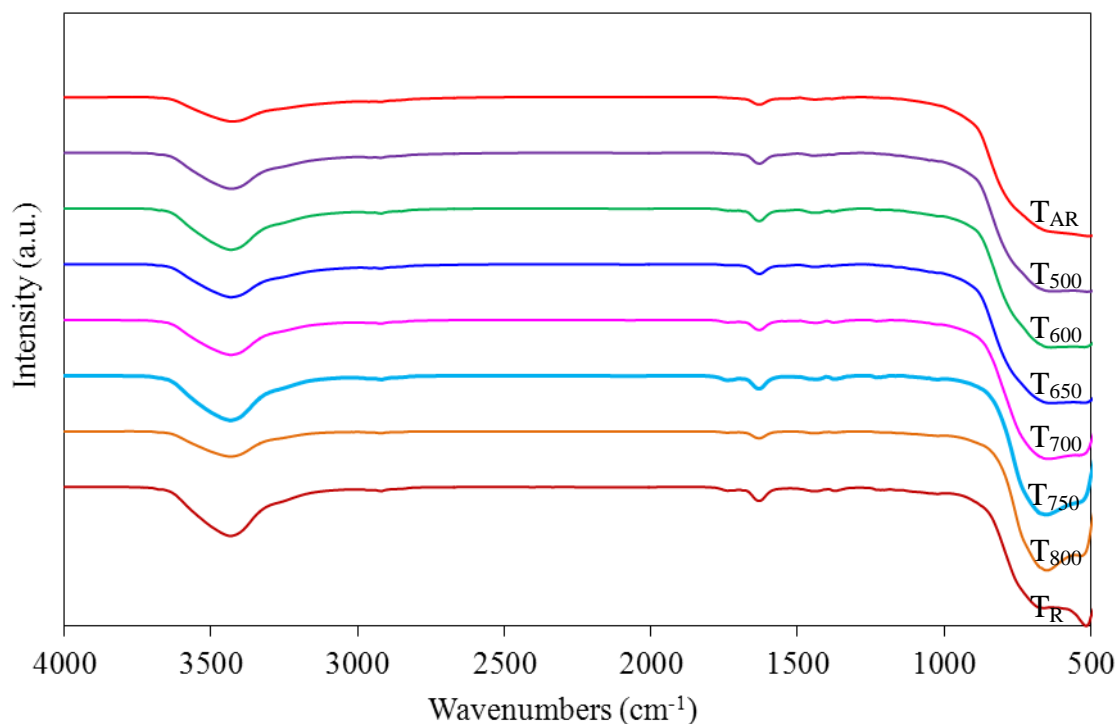


Figure 2. Representative FT-IR of the commercial TiO_2 samples (T_{AR} and T_{R}) and the TiO_2 after treatment at different temperatures ($T_{500-800}$).

Table 2. Morphology of the Pt/C, PtPd/C and the different TiO_2 -PtPd/C catalysts.

Catalysts	d -value (nm)	Lattice parameter (nm)	Pt: Pd: Ti (atomic ratio)	Crystal size (nm)	Dispersion (N_s/N_T %)	ECSA (m^2/g)	Conductivity (S/cm)	Contact angle (degree)
Pt/C	0.1387	0.3954	100: 0: 0	7.66	17.0	13.24	26.97	137
PtPd/C	0.1379	0.3901	36: 64: 0	6.20	20.1	16.67	17.96	140
T_{AR} -PtPd/C	0.1375	0.3890	34: 61: 5	6.37	19.9	5.36	16.07	145
T_{500} -PtPd/C	0.1382	0.3909	33: 58: 9	6.58	19.4	5.22	38.18	145
T_{600} -PtPd/C	0.1385	0.3817	37: 58: 5	6.57	19.5	6.53	40.06	146
T_{650} -PtPd/C	0.1378	0.3896	35: 60: 5	6.65	19.1	6.78	40.16	146
T_{700} -PtPd/C	0.1378	0.3897	33: 60: 7	6.64	19.4	9.58	45.00	148
T_{750} -PtPd/C	0.1377	0.3895	34: 61: 5	6.63	19.2	9.70	47.69	149
T_{800} -PtPd/C	0.1381	0.3907	34: 63: 3	6.50	19.4	11.23	53.09	154
T_{R} -PtPd/C	0.1377	0.3900	35: 62: 3	6.94	18.4	12.15	22.89	149

The surface property of TiO_2 before and after thermal treatment was qualitative monitored by using the FT-IR spectroscopy. As demonstrated in Fig.2, the broad band at $3,300\text{-}3,700\text{ cm}^{-1}$ and peak at $1,630\text{ cm}^{-1}$ refer to the surface-adsorbed water and hydroxyl groups, respectively [34]. Main peak at

400-710 cm^{-1} was designated as Ti-O stretching and Ti-O-Ti bridging stretching modes [35]. Quantitatively, the untreated T_{AR} had quantity of surface hydroxyl groups of about 3.57 mEq/g, which was greater than that of T_R of around 2.5 times (Table 1). As the increasing treatment temperature for T_{AR} , the quantity of hydroxyl groups decreased importantly. This was probably due to the decrease of BET surface areas and pore volume, causing the reduction of the adsorbed water [36].

The representative XRD patterns of different catalyst samples were shown in Fig. 3. All the PtPd/C catalysts (with and without TiO_2) revealed peaks at a 2θ of around 40.04° , 46.60° and 67.3° , which were assigning to the face-centered cubic (FCC) structure of Pt at the [111], [200] and [220] planes, respectively.

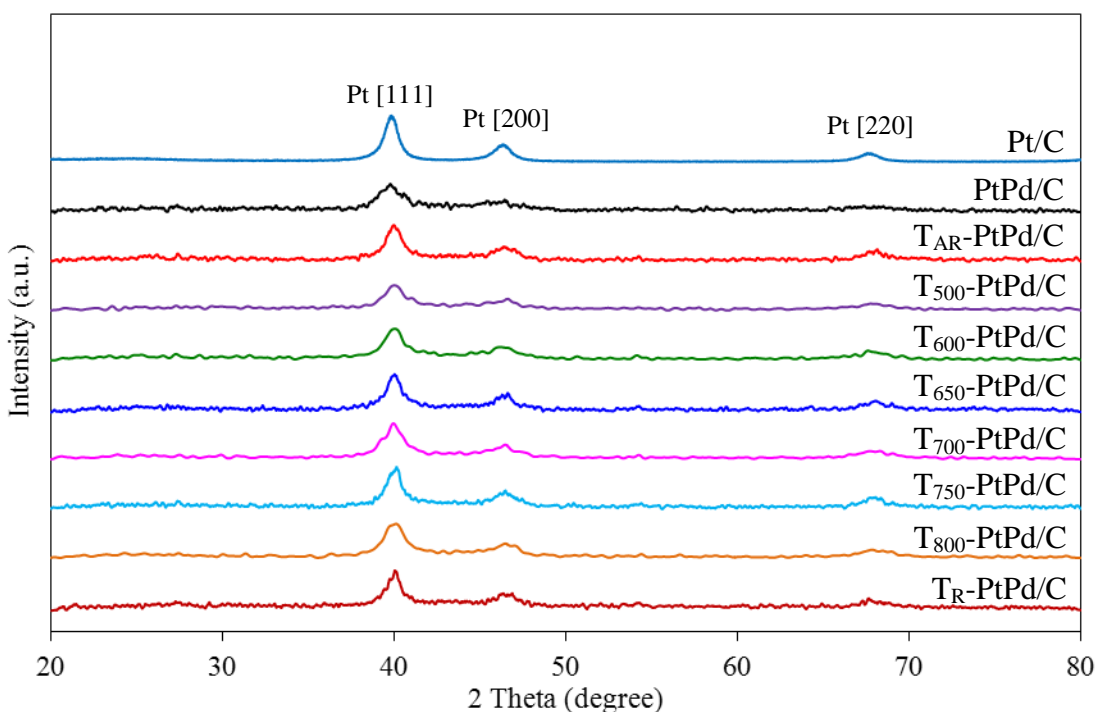


Figure 3. Representative XRD patterns of the Pt/C, PdPt/C and the different TiO_2 -PtPd/C catalysts.

Compared with the XRD pattern of the bulk Pt/C catalyst, these diffraction peaks were shifted to slightly higher 2θ values, suggesting the formation of the Pt-Pd alloy in the presence or absence of TiO_2 in the catalyst layer. The formation of the Pt-Pd alloy was also supported by the decreased lattice parameters and d -value of the PtPd/C and TiO_2 -PtPd/C catalysts compared with the Pt/C catalyst (Table 2), caused by the particle substitution of Pt by Pd in the FCC structure. Interestingly, no characteristic peaks of TiO_2 were observed in the XRD peaks of all the TiO_2 -PtPd/C catalysts, which is probably due to the proportionally very small quantity of TiO_2 in these catalysts. However, the existence of TiO_2 , as well as Pd, was confirmed using SEM-EDX analysis (figure not shown), where the average atomic ratios of Pt: Pd: Ti in the TiO_2 -PtPd/C catalysts were at around 34.1: 60.7: 5.2 (Table 2).

From the analysis using the Debye-Scherrer equation, the PtPd/C catalyst had a smaller grain size than the Pt/C catalyst, which was attributed to the fact that more Pd can enter into the lattice of Pt.

This has been reported previously for Pt-M catalysts where M = Fe, Co, Ni and Cu [5,37]. The incorporation of TiO₂ on the catalyst layer did not alter the crystal size of PtPd catalysts significantly. Their sizes fluctuated around 6.37–6.65 nm, slightly greater than that of PtPd/C catalyst, but still smaller than that of the Pt/C catalysts. In addition, a higher level of particle dispersion, as estimated by the polynomial equations shown in Eqs. (2)-(4) [38], was fluctuated in the narrow range of 19.1–19.9%, which was higher than that of the Pt/C catalyst.

$$N_T = \frac{2\pi}{3} \left(\frac{D}{a} \right)^3 \quad (2)$$

$$N_T = \left(\frac{10}{3} \right) l^3 - 5l^2 + \left(\frac{11}{3} \right) l - 1 \quad (3)$$

$$N_S = 10l^2 - 20l + 12 \quad (4)$$

where N_T is the total number of atoms, N_S is the number of surface atoms, l is the number of layers, D is the average particle size and a is the lattice parameter.

The ECSA of the PtPd/C catalysts was determined by the H₂ stripping method. A well-defined cyclic voltammogram of all Pt/C, PtPd/C and also TiO₂-PtPd/C catalyst was observed. As an example, the adsorption peak of Pt-OH and Pt-O was observed as a shoulder peak at a potential of 0.6–0.9 V in the forward scan (Fig.4).

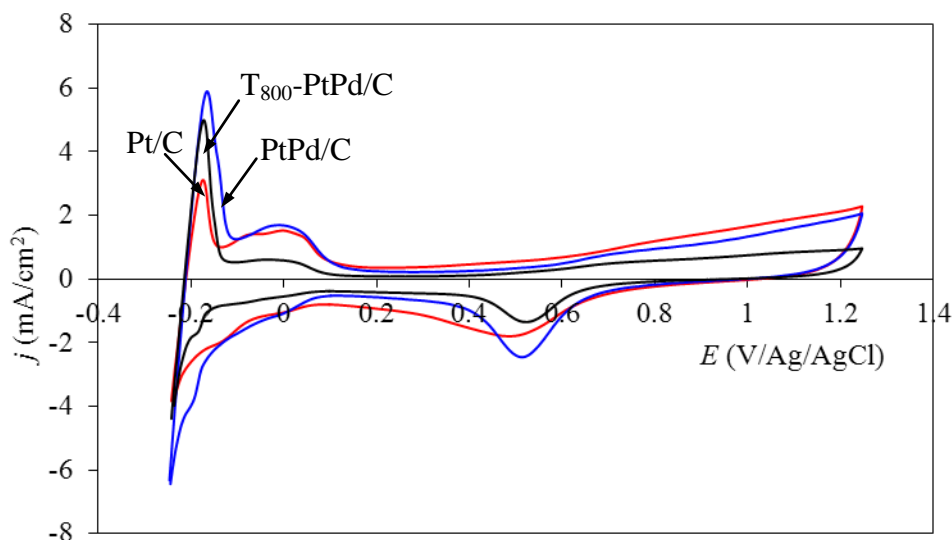


Figure 4. Representative cyclic voltammogram of the Pt/C, PtPd/C and T₈₀-PtPd/C catalysts.

The evolution of O₂, generated from H₂O oxidation, was not observed in this case because it probably required a more positive potential. In the reverse scan, the adsorption of -O from the Pt surface (Pt-O) appeared at 0.52 V, while the adsorption peak of the H atom on the Pt surface (Pt-H) was evident at a potential of 0.1 to -0.2 V. The marked increase in the current density at a potential of less than -0.2 V was attributed to H₂ evolution by H⁺ or H₂O reduction. When the cell potential was reversed again, two desorption peaks of H atoms from the Pt surface were observed with peak potentials of -0.2 V and 0.0 V that correspond to the desorption of H atoms from the Pt[110] and

Pt[100] crystalline planes, respectively. From this voltammogram, the area under the hydrogen desorption peak was used to calculate the ECSA according to Eqs. (5) and (6) [39];

$$ECSA = \frac{Q}{[M] \times 0.21}, \quad (5)$$

$$Q = \frac{1}{\nu} \int_{-0.2}^{0.1} (j - j_{dl}) dE, \quad (6)$$

where Q is the charge used to desorb hydrogen from a catalyst surface (Eq. (6)), $[M]$ is the catalyst loading, ν is the scan rate, j is the current density, j_{dl} is the current density at the double layer region and E is the potential.

The PtPd/C catalyst exhibited a higher ECSA than the Pt/C catalyst (Table 2), which is due to its small crystal size and high catalyst dispersion. Incorporation of TiO_2 in the PtPd/C catalyst layer decreased the ECSA, which was probably due to the partial coverage of the PtPd/C catalyst by the corresponding TiO_2 that reduced the available active area for the reaction. However, the magnitude of the decreased ECSA upon incorporation of TiO_2 was inversely dependent upon the TiO_2 treatment temperature. This might reflect the effect of the different crystal sizes of the incorporated TiO_2 on the electrode roughness, where TiO_2 prepared at a high treatment temperature had a larger crystal size that induced a higher level of electrode roughness, and so resulted in a higher accessibility of the reactant to the catalyst active sites.

The hydrophobic and hydrophilic properties of the prepared catalysts were determined in terms of the water contact angle, where a high water contact angle is ascribed to a high hydrophobic property of that surface [16]. The addition of TiO_2 to the PtPd/C catalyst increased the water contact angle in a treatment temperature-dependent manner (Table 2). Thus, the T_{80} -PtPd/C catalyst exhibited the highest water contact angle of 154° , suggesting its highest hydrophobicity, which is attributed to the low level of surface -OH groups on the surface of T_{800} (Table 1).

3.2. ORR activity of TiO_2 -PtPd/C catalysts

The ORR activities of the TiO_2 -PtPd/C catalysts were first tested in oxygen-saturated H_2SO_4 (0.5 M) at constant scan rate of 10 mV/s with different rotation rates (500–2,000 rpm). A similar pattern of a well-defined mass transfer and kinetic control regions was observed for all the PtPd catalysts (Fig. 5(a)), where the kinetic control region (the region where the rotation rate and the mass transport do not affect the current density) was above 0.70 V in all the catalysts. Within the 0.55 to 0.70 V region, changes in the current density showed a non-linear relationship with respect to the rotation rate ($\omega^{1/2}$), and so represented a mixed kinetic-diffusion control reaction. The diffusion control region, where the current density changed linearly with the rotation rate ($\omega^{1/2}$) and reached its plateau was at the potential lower than 0.6 V. Increasing the rotation rate of the disc electrode increased the limiting current due to the increased availability of oxygen at the electrode surface [33].

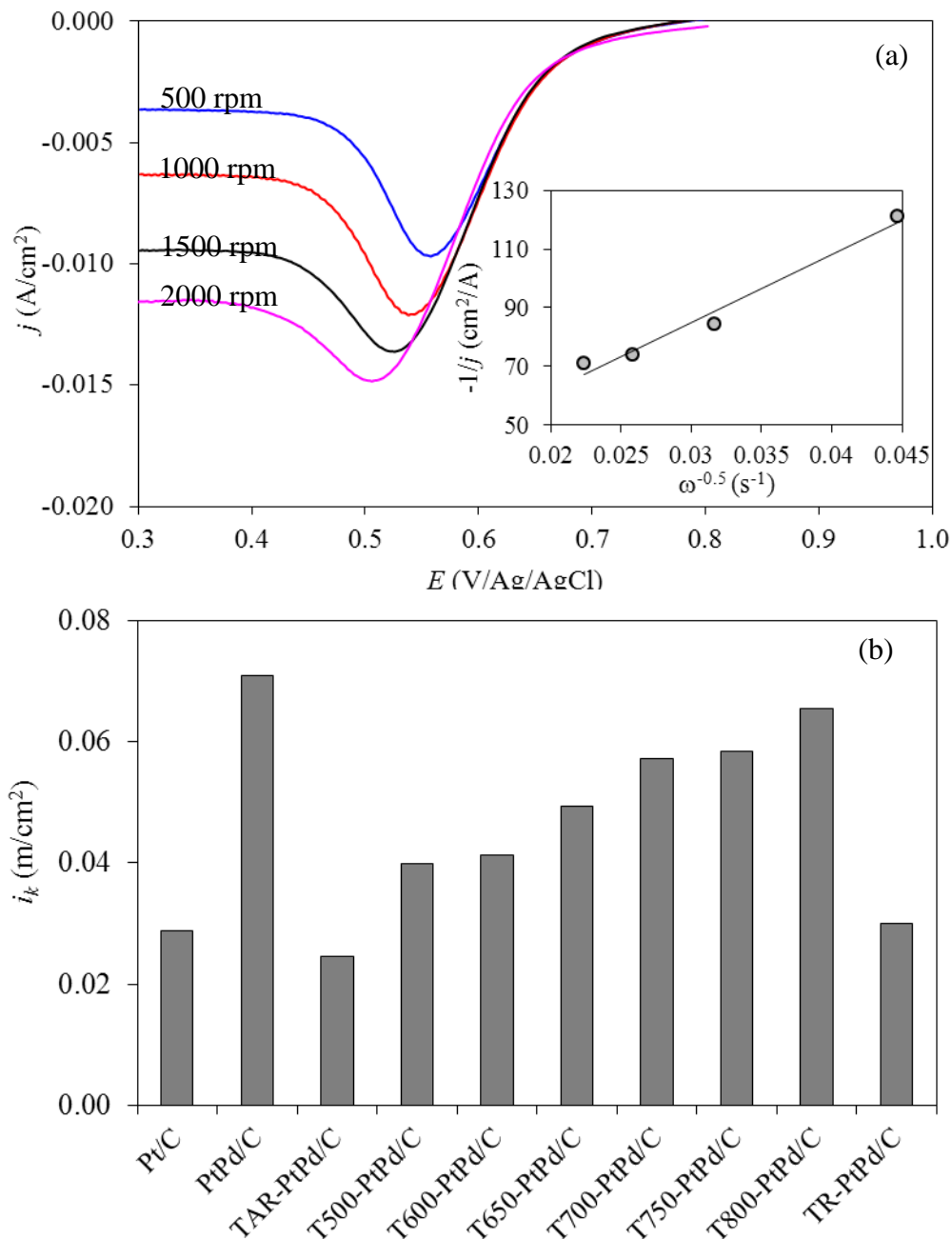


Figure 5. (a) The LSV curves for the T₈₀₀-PtPd/C catalysts at different rotation rates in oxygen-saturated 0.5 M H₂SO₄ at 25 °C with a scan rate of 10 mV/s and the insert is example plot of j^{-1} vs. $\omega^{-1/2}$ used to determine the number of electrons transferred in the process and i_k (b) The kinetically controlled ORR current at 0.54 V for the Pt/C, PtPd/C and the different TiO₂-PtPd/C catalysts.

Based on the assumption of first-order kinetics with respect to the oxygen concentration, the current density related to the rotation rate is expressed by the Levich-Koutecky equation [40], as shown in Eqs. (7) and (8):

$$\frac{1}{j} = \frac{1}{j_k} + \frac{1}{B\sqrt{\omega}}, \tag{7}$$

$$\text{where} \quad B = 0.62nFD^{2/3}\nu^{-1/6}C. \quad (8)$$

Here, j_k is the mass transport free kinetic current density, ω is the rotation rate, n is the number of involved electrons, F is the Faraday's constant (96,485 C/mol), D is the diffusion coefficient of oxygen in solution (1.9×10^{-5} cm²/s), ν is the kinematics viscosity (0.01 cm²/s) and C is the oxygen concentration in the bulk solution (1.1×10^{-6} mol/cm³).

The plot of j^{-1} vs. $\omega^{-1/2}$ has the slope $1/B$, which was then used to determine the number of electrons transferred in the process (insert of Fig.5(a)). From the calculation, the number of involved electrons for the ORR of the PtPd/C catalyst was 3.99 and those of the TiO₂-PtPd/C catalysts varied between 3.67 and 4.00, indicating that the ORR on the PtPd/C and TiO₂-PtPd/C catalysts involved the four-electron pathway. Also, the kinetic currents (j_k) obtained from the intercept of this curve were used to determine the ORR activity [41]. As shown in Fig. 5(b), the PtPd/C catalyst exhibited a higher i_k value (and so a higher ORR activity) compared with that for Pt/C. This was attributed to the effect of Pt-Pd alloy formation as well as its lower particle size, and higher catalyst dispersion and ECSA. The incorporation of TiO₂ in the PtPd/C catalyst layer reduced the i_k value markedly, although the magnitude of this reduction was inversely proportional to the TiO₂ treatment temperature, which reflects the low BET surface area of the TiO₂-PtPd/C catalysts compared to the original PtPd/C catalyst. Thus, among the TiO₂-PtPd/C catalysts, the ORR activity increased with increasing TiO₂ treatment temperature and so might depend on the TiO₂ phase in the catalyst layer. That is, TiO₂ with a high rutile content induced a higher ORR activity in the PtPd/C catalyst than those with a lower rutile phase content, which is consistent with some previous reports [33]. However, this is not exactly true for the T₈₀₀-PtPd/C and T_R-PtPd/C catalysts, where they had an almost similar rutile content (~ 99%) and ECSA (11.23 and 12.15 m², respectively) as each other but T₈₀₀-PtPd/C provided a three-fold greater ORR activity than the T_R-PtPd/C catalyst. This might be due to the difference in their phase structure, where the T₈₀₀-PtPd/C catalyst exhibited sharper rutile peaks, suggesting a higher degree of crystallinity, than the T_R-PtPd/C catalyst (Fig. 1). The higher crystallinity level can promote the generation of an electron-conducting network in the electrode and consequentially an increased electrical conductivity (Table 2). In addition, a high treatment temperature can induce a high level of electron mobility along the TiO₂ structure due to the thermal activation that results in a high total electrical conduction [42]. Accordingly, the ORR activity of the TiO₂-PtPd/C catalyst appears to be dependent on the ESCA and the conducting network in the catalyst layer. To monitor the activity of catalysts in an actual application, each of the prepared TiO₂-PtPd/C catalysts was used as a cathode in a PEM fuel cell and tested under a H₂/O₂ environment. The open circuit potential (OCP) of the PtPd/C catalyst and all the TiO₂-PtPd/C catalysts were nearly the same (Fig. 6). A slight difference in the performance loss was observed at a low current density (during the activation polarization region) but a marked drop in the cell performance occurred during the medium-to-high current density. In Fig. 6(a), the current densities of the PtPd/C catalysts were ranked in the order of T₈₀₀-PtPd/C > PtPd/C > T_R-PtPd/C > Pt/C at 0.6 V. At $E < 0.6$ V, the cell performance of the PtPd/C and T_{AR}-PtPd/C catalysts started to deviate away from linearity and drastically drop to a potential of less than 0.3 V. A similar drop in the cell performance during the medium-to-high potential was observed with the TiO₂-PtPd/C catalysts (Fig. 6(b)), but the T₈₀₀-PtPd/C catalyst still had the highest current density of 486 mA/cm² (291 mW/cm²) at 0.6 V.

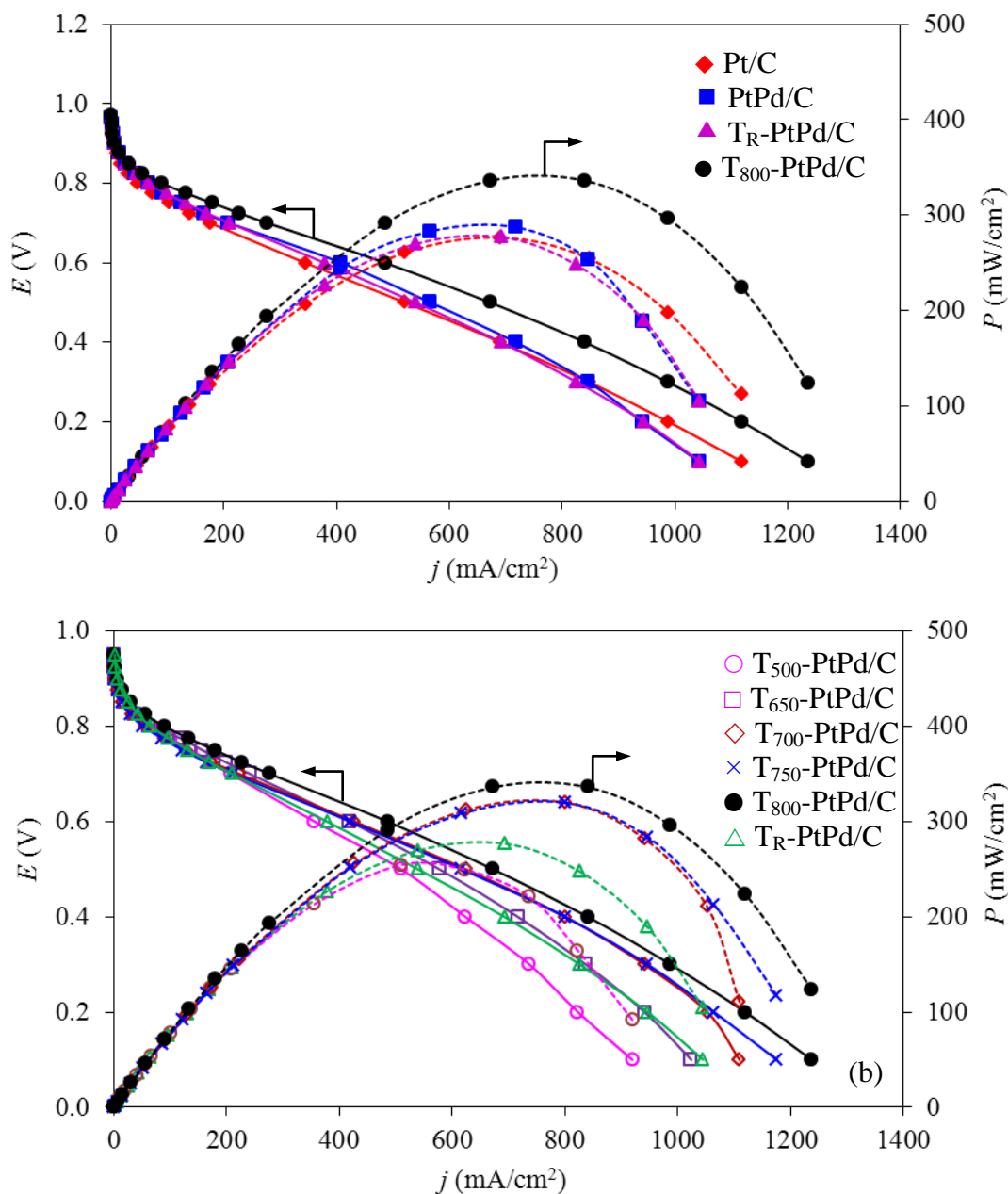


Figure 6. Representative (—) current density-potential curve and (.....) current density-power density of a single H₂/O₂ PEM fuel cell at atmospheric pressure (1.0 psia) for the different TiO₂-PtPd/C catalysts.

Theoretically, the loss of cell performance during a medium-to-high current density in PEM fuel cells has been attributed to various factors, including (i) the sluggish electron transfer through the electrically conductive fuel cell components, such as the catalyst layer, interconnector, flow field plate/bipolar plate, and so on, and (ii) the sluggish ion (H⁺) transfer through the electrolyte. The higher cell performance of the T₈₀₀-PtPd/C catalyst than that of the other investigated catalysts might be attributed to its high electrical conductivity (Table 2). In addition, the departure in the cell performance from linearity at a medium-to-high current density can be attributed to mass-transport limitations,

caused by either a change in the porosity and/or tortuosity in the diffusion layer of the electrode or by the presence of water droplets or films in the diffusion layer [43]. The marked performance drop of the PtPd/C and T_{AR}-PtPd/C catalyst at a low potential ($E < 0.6$ V), where a high current density was drawn (Fig.6(a)), might be due to mass-transport limitation caused by the accumulation of generated water droplets on the catalyst surface that hinders the accessibility of the reactant to the reaction site. The incorporation of highly hydrophobic substances (or TiO₂ in this case) in the catalyst layer can alleviate the mass-transport limitation. As demonstrated in Fig.6(b), the T₈₀₀-PtPd/C catalyst was still exhibited the highest cell performance compared with other TiO₂-PdPt/C catalysts. This is because it had the highest water contact angle or the highest hydrophobicity and so was the least susceptible catalyst to water flooding compared to the other catalysts.

4. CONCLUSIONS

A series of TiO₂ samples were prepared by thermal treatment at different temperatures and then incorporated in cathode PtPd/C catalyst layer of a PEM fuel cell to improve the ORR activity and water management aspect. The treatment temperature affected the morphology as well as properties of the obtained TiO₂ powder and also the ORR activity of TiO₂-PtPd/C catalysts. Although the TiO₂ prepared at 800 °C (T₈₀₀) had the lowest BET surface area of the TiO₂ samples, due to its larger particle size, it promoted a higher ECSA and electrical conductivity as well as hydrophobic properties of the PtPd/C catalyst layer. These positively influence the ORR activity of the T₈₀₀-PtPd/C catalyst in both an acid solution and in a PEM fuel cell under a H₂/O₂ environment.

ACKNOWLEDGMENTS

The project was funded by the Ratchadapisek Sompoch Endowment Fund, Chulalongkorn University (Sci-Super 2014-027) and the Chulalongkorn University Graduate School Thesis Grant. Also, we thank the Publication Counseling Unit (PCU) of the Faculty of Science, Chulalongkorn University, and Dr. Robert D.J. Butcher for comments, suggestions and checking the grammar.

References

1. F. Barbir, PEM fuel cells: Theory and Practice. 2nd edition. Elsevier Inc. London, UK. 2013.
2. X.Z. Yuan, H. Wang H, PEM fuel cell Fundamentals, in PEM fuel cell electrocatalysts and catalyst layers: Fundamentals and Applications. Edited by Zhang J. Springer-Verlag London Ltd. 2008.
3. X. Zhang, J. Guo, J. Chen, *Energy*, 35 (2010) 5294.
4. M. Min, J. Cho, K. Cho, H. Kim, *Electrochim. Acta*, 45 (2000) 4211.
5. L. Xiong, A.M. Kannan, A. Manthiram, *Electrochem. Commun.*, 4 (2002) 898.
6. J. Luo, P.N. Njoki, Y. Lin, L. Wang, C.J. Zhong, *Electrochem. Commun.*, 8 (2006) 581.
7. J.F. Whitacre, T.I. Valdez, S.R. Narayanan, *Electrochim. Acta*, 53 (2008) 3680.
8. C. Termpornvithit, N. Chewasatn, M. Hunsom, *Appl. Electro.*, 42 (2012) 169.
9. S. Limpattayanate, M. Hunsom, *Renew. Energ.*, 63 (2014) 205.
10. S. Mukerjee, S. Srinivasan, M.P. Soriaga, J. McBreen, *J. Electrochem. Soc.*, 142 (1995) 1409.

11. H. Beydaghi, M. Javanbakht, H.S. Amoli, A. Badiei, Y. Khaniani, M.R. Ganjali, P. Norouzi, M. Abdouss, *Int. J. Hydrogen Energ.*, 36 (2011) 13310.
12. A. Iulianelli, I. Gatto, F. Trotta, M. Biasizzo, E. Passalacqua, A. Carbone, A. Bevilacqua, G. Clarizia, A. Gugliuzza, A. Basile, *Int. J. Hydrogen Energ.*, 38 (2013) 551.
13. K.S. Yoon, J.Y. Lee, T.H. Kim, D.M. Yu, D.W. Seo, S.K. Hong, Y.T. Hong, *J. Ind. Eng. Chem.*, 20 (2014) 2310.
14. M. Malinowski, A. Iwan, K. Parafiniuk, L. Gorecki, G. Pasciak, *Int. J. Hydrogen Energ.*, 40 (2015) 833.
15. G. Hoogers, Fuel cell component and their impact on performance, in Fuel cell technology handbook, edited by Hoogers G., CRC Press, Washington, D.C., 2003.
16. S. Park, J.W. Lee, B.N. Popov, *J. Power Source*, 177 (2008) 457.
17. J.H. Nam, M. Kaviani, *Int. J. Heat Mass Transfer*, 46 (2003) 4595.
18. A.Z. Weber, R.M. Darling, J. Newman, *J. Electrochem. Soc.*, 151 (2004) A1715.
19. T. Ous, C. Arcoumanis, *J. Power Source*, 173 (2007) 137.
20. J.G. Carton, V. Lawlor, A.G. Olabi, C. Hochenauer, G. Zaune, *Energy*, 39 (2012) 63.
21. S. Endoo, K. Pruksathorn, P. Piumsomboon, *Renew. Energy*, 35 (2010) 807.
22. E. Passalacqua, F. Lufrano, G. Squadrito, A. Patti, L. Giorgi, *Electrochim. Acta*, 46 (2001) 799.
23. E. Antolini, L. Giorgi, A. Pozio, E. Passalacqua, *J. Power Source*, 77 (1999) 136.
24. A. Fujishima, K. Hashimoto, T. Watanabe, *TiO₂, Photocatalysis, Fundamentals and Applications*, BKC, Inc., Tokyo, 1999.
25. A.Š. Vuk, R. Ješe, B. Orel, G. Dražić, *Int. J. Photoenergy*, 7 (2005) 163.
26. A. Davydov, *Molecular Spectroscopy of Oxide Catalyst Surfaces*, John Wiley, New York, 2003.
27. K.I. Hadjiivanov, D.G. Klissurski, *Chem. Soc. Rev.*, 25 (1996) 61.
28. W. Trongchuanvij, K. Poochinda, K. Pruksathorn, H. Hunsom, *Renew. Energy*, 12 (2010) 2839.
29. S. Thanasilp, M. Hunsom, *Electrochim. Acta*, 56(2011) 1164.
30. S. Thanasilp, M. Hunsom, *Fuel*, 89 (2010) 3847.
31. C.H. Tessmer, R.D. Vidic, L.J. Uranowski, *Environ. Sci. Technol.*, 31 (1997) 1872.
32. X. Chen, S. Jeyaseelan, N. Graham, *Waste Manage*, 22 (2002) 755.
33. S.Y. Huang, P. Ganesan, B.N. Popov, *Appl. Catal. B-Environ*, 96 (2010) 224.
34. G. Wang, L. Xu, J. Zhang, T. Yin, D. Han, *Int. J. Photoenerg.*, (2012) Article ID 265760: 1-9.
35. J.G. Yu, Y.R. Su, B. Cheng, M. Zhou, *J. Mol. Catal. A: Chem.*, 258 (2006) 104.
36. J.G. Yu, H.G. Yu, *Mater. Chem. Phys.*, 100 (2006) 507.
37. H. Wu, D. Wexler, G. Wang, *J. Alloy Compd.*, 488 (2009) 195.
38. J.J. Van Der Klink, *Adv. Catal.*, 44 (1999) 1.
39. S. Yin, S. Mu, H. Lv, N. Cheng, M. Pan, Z. Fu, *Appl. Catal. B.*, 93 (2010) 233.
40. A.J. Bard, L.R. Faulkner, *Electrochemical methods: fundamentals and applications*. New York: Wiley (2001).
41. S.Y. Huang, P. Ganesan, B.N. Popov, *ACS Catal.*, 2 (2012) 825.
42. A. Uygun, O. Turkoglu, S. Sen, E. Ersoy, A.G. Yavuz, G.G. Batir, *Curr. Appl. Phys.*, 9 (2009) 866.
43. J. Kim, S.M. Lee, S. Srinivasan, C.E. Chamberlin, *J. Electrochem. Soc.*, 142 (1995) 2670.